Noise-assisted transport mechanism analysis and synaptic characteristics in ZrO$_x$/HfAlO$_x$-based memristor for neuromorphic systems

Jungang Heo ⑩ ; Youngboo Cho; Hyeonseung Ji; Min-Hwi Kim; Jong-Ho Lee ⑩ ; Jung-Kyu Lee ✉ ⑩ ; Sungjun Kim ✉ ⑩

Check for updates

View Online   Export Citation   CrossMark

AIP Publishing

Noise-assisted transport mechanism analysis and synaptic characteristics in ZrO_X/$HfAlO_X$-based memristor for neuromorphic systems

View Online   Export Citation   CrossMark

Jungang Heo,[1] (iD) Youngboo Cho,[1] Hyeonseung Ji,[1] Min-Hwi Kim,[2] Jong-Ho Lee,[3] (iD) Jung-Kyu Lee,[1,a] (iD) and Sungjun Kim[1,a] (iD)

AFFILIATIONS

[1] Division of Electronics and Electrical Engineering, Dongguk University, Seoul 04620, South Korea
[2] School of Electrical and Electronics Engineering, Chung-Ang University, Seoul 06974, Republic of Korea
[3] Department of Electrical and Computer Engineering and Inter-University Semiconductor Research Center, Seoul National University, Seoul 08826, Republic of Korea

[a] Authors to whom correspondence should be addressed: jungkyu0712@gmail.com and sungjun@dongguk.edu

ABSTRACT

In this work, we compare the resistive switching characteristics between Ti/ZrO_X/TiN and Ti/ZrO_X/$HfAlO_X$/TiN. The bilayer structure of the ZrO_X-based device enables power consumption reduction owing to a lower forming voltage and compliance current. Moreover, the on/off ratio of the Ti/ZrO_X/$HfAlO_X$/TiN device ($>10^2$) is higher than that of the Ti/ZrO_X/TiN device (>10). We use the $1/f$ noise measurement technique to clarify the transport mechanism of the Ti/ZrO_X/$HfAlO_X$/TiN device; consequently, ohmic conduction and Schottky emission are confirmed in the low- and high-resistance states, respectively. In addition, the multilevel cell, potentiation, and depression characteristics of the Ti/ZrO_X/HfO_X/TiN device are considered to assess its suitability as a neuromorphic device. Accordingly, a modified National Institute of Standards and Technology database simulation is conducted using Python to test the pattern recognition accuracy.

I. INTRODUCTION

The explosive growth of data in recent years has resulted in numerous challenges for traditional computing systems that are based on the von Neumann architecture.[1] These systems rely on a centralized processing unit to execute instructions and access data stored in the memory. However, as the amount of data continues to increase, this approach has become a bottleneck as it requires a significant amount of time and energy to move data between the processing unit and memory.[2] This challenge has motivated the development of novel computing architectures that can overcome these limitations. In this context, neuromorphic computing has emerged as a promising alternative, inspired by the architecture and functionality of the human brain.[3] Neuromorphic computing systems are designed to mimic the parallel processing and distributed memory capabilities of the human brain, enabling them to perform tasks such as pattern recognition and decision-making with remarkable efficiency. In recent years, numerous emerging memory technologies have been investigated for their potential in neuromorphic applications, including phase-change random-access memory (PRAM), ferroelectric random-access memory (FRAM), magnetic random-access memory (MRAM), and spin-transfer torque MRAM (STT-MRAM).[4–7] PRAM stores data by changing the phase of a chalcogenide material using heat, while FRAM uses a ferroelectric material to store data through polarization. MRAM and STT-MRAM rely on magneto-resistive effects to store data by changing the magnetic orientation of a thin-film element. Among the emerging memory technologies, resistive random-access memory (RRAM) is a promising candidate for neuromorphic applications owing to its properties of high speed, low power consumption, and high scalability. Because of its straightforward design and CMOS process compatibility, RRAM is also easily scalable and simple to

29 November 2023 01:37:43

integrate with existing electronic systems.[8] RRAM is a non-volatile memory device that utilizes metal oxide layers to store information. Among the various metal oxide materials, TiO_X, TaO_X, NiO_X, ZnO, AlO_X, ZrO_X, and HfO_X have extensively been studied for their RRAM applications.[9–15] When metal oxides are used as insulators, resistive switching (RS) can occur owing to the presence of oxygen vacancies, which can form conducting filaments (CFs). These filaments can be broken by binding with oxygen ions, resulting in resistive switching. Therefore, the distribution of oxygen vacancies and ions significantly affects RS.[16]

Utilizing a bilayer structure in RRAM devices has been demonstrated to enhance RS properties because of regulated oxygen vacancy movements from the bilayer interface. This reduces the variability in resistivity, leading to more stable performance overall. Moreover, the bilayer configuration improves durability and reliability by enhancing information retention.[17] Ye *et al.* revealed that the multilevel RS behaviors of HfO_2/TiO_2 bilayer structures exhibit excellent uniformity, high durability, and exceptional mechanical flexibility.[18] Lee *et al.* found that ZrO_X/HfO_X bilayer-structured devices display great data retention at 85 °C, uniform distribution of the switching characteristics, strong switching endurance up to 10^5 cycles, and lower reset currents.[19] Previous research has shown that $HfAlO_X$-based RRAM devices demonstrate superior properties, such as large windows for resistance states, uniformity, and endurance, making them promising options for synaptic devices. Sokolov *et al.* reported that $Ti/HfAlO_X/Pt$ RRAM devices achieve uniform and higher self-compliant RS behaviors.[20] Ryu *et al.* reported a $Pt/HfAlO_X/TiN$ memristor device design with voltage-controlled synaptic behaviors and current sweeping mode for neuromorphic applications.[21] Lin *et al.* reported that abundant oxygen vacancy exists in the ZrOx layer and that it has a hysteresis curve.[22] Surazhevsky *et al.* reported that $Au/ZrO_2/TiN$ devices have large on/off ratios and stable switching. In addition, it was found to be a suitable device for learning using spike-timing-dependent plasticity (STDP).[23]

In the present study, a bilayer device was manufactured by atomic layer deposition (ALD) with 1.5 nm thick $HfAlO_X$ at the ZrO_X/TiN interface. The bilayer device was operated with a lower compliance current (I_{cc}) than the single-layer device, allowing better control over the formation of CFs. This resulted in a lower conductance value for the bilayer device, which is beneficial in terms of power consumption. The RS mechanism was confirmed through the oxygen vacancy scheme. To clarify the transport mechanism in the RRAM device, we adopted a diagnosis tool involving $1/f$ noise measurement. The $1/f$ noise degrades the performance and stability of circuit systems and is one of the most critical limiting factors in circuit design. However, interestingly, $1/f$ noise analysis is a fast, repeatable, and nondestructive electrical characterization technique that analyzes the characteristics of devices such as working principle, transport mechanism, and trap analysis.[24–27] The compliance current and reset voltage were modulated to produce the multilevel RS characteristics. Furthermore, long-term potentiation and depression were attained both consistently and repeatedly. Accordingly, a modified National Institute of Standards and Technology (MNIST) database simulation was conducted using Python to test the pattern recognition accuracy.

II. EXPERIMENTS

A. Device fabrication

The RRAM devices were fabricated as follows: First, a 100 nm-thick TiN layer was deposited on a SiO_2/Si substrate wafer via reactive sputtering in the presence of gaseous N_2 and Ar. In the $Ti/ZrO_X/HfAlO_X/TiN$ device, a 1.5 nm $HfAlO_X$ layer was deposited by ALD technology using tetrakis (ethylmethylamido) hafnium (TEMAHf) and trimethyl aluminum (TMA) as Hf and Al precursors, respectively, and ozone (O_3) was used as an oxidant. ZrO_X switching layers were subsequently deposited to a thickness of 20 nm using reactive sputtering at room temperature. Then, a 20 nm-thick Ti top electrode was deposited on the ZrO_X/TiN and $ZrO_X/HfAlO_X/TiN$ substrates by DC magnetron sputtering. Finally, a Pt capping layer was deposited to prevent the oxidation of Ti when in contact with air.

B. Electrical measurement

The I–V and transient curves of the RRAM cells were obtained by measurements using a semiconductor parameter analyzer (Keithley 4200-SCS and 4225-PMU ultrafast current–voltage modules, Keithley Instruments, Cleveland, OH, USA). A bias was applied to the Ti top electrode, and the TiN bottom electrode was grounded. The $1/f$ noise characteristics were analyzed using a low-noise current amplifier (SR570) and a signal analyzer (35670A). The schematic diagram of the $1/f$ noise measurement system is shown in Fig. S1 (the supplementary material). The voltage applied to the top electrode was supplied by a semiconductor parameter analyzer (B1500A). The output current of the RRAM device was connected to the SR570 to convert the current fluctuations into voltage fluctuations. The 35670A then converted the dynamic signal from the SR570 into a power spectral density. The noise floor of our measurement system is $\sim 10^{-24}$ A^2/Hz, significantly lower than the device noise. This ensures that the noise power spectral density measured in this study is not affected by the measurement system noise floor.

III. RESULTS AND DISCUSSION

A. Material characterization and surface analysis

The $Ti/ZrO_X/HfAlO_X/TiN$ RRAM device stack is shown schematically in Fig. 1(a) and matches the transmission electron microscopy (TEM) image in Fig. 1(b). The amorphous ZrO_X layer is around 20 nm thick, and a clear interface is visible between the TiO_X and Ti/ZrO_X layers because the Ti top electrode is partially oxidized during deposition, creating a 7 nm-thick TiO_X layer. In addition, a 1.5 nm-thin $HfAlO_X$ layer was applied by ALD at the TiN/ZrO_X interface. The chemical composition analysis of ZrO_X and $HfAlO_X$ was meticulously performed using x-ray photoelectron spectroscopy (XPS) with a Nexsa G2 surface analysis system from Thermo Fisher Scientific. The detected peak positions were calibrated by performing Shirley background subtraction using the photoemission signal of the C 1s (284.6 eV). Subsequently, 5% Gaussian–Lorentzian functions were utilized to fit the XPS spectra. The high-resolution
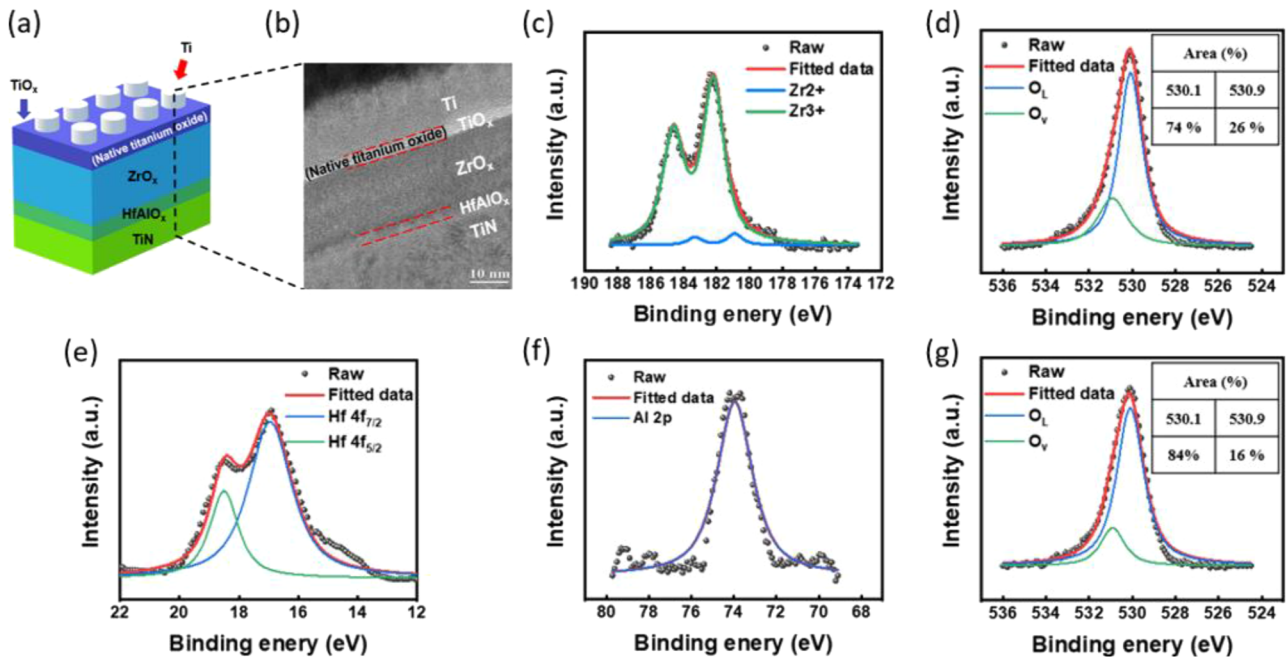
FIG. 1. (a) Schematic illustration of Ti/TiO$_X$/ZrO$_X$/HfAlO$_X$/TiN. (b) Cross-sectional TEM view of the Ti/TiO$_X$/ZrO$_X$/HfAlO$_X$/TiN RRAM device. X-ray photoelectron spectroscopy results of (c) Zr 3d, (d) O 1s at ZrO$_X$, (e) Hf 4f, (f) Al 2p, and (g) O 1s at HfAlO$_X$.

spectrum of the ZrO$_X$ layer was presented in Fig. 1(c), and it was observed that the Zr 3d doublet could be divided into two groups of peaks corresponding to Zr in the metallic state (Zr^0) at 178.7 eV and to a sub-oxide (Zr^{1+}) located at 179.8 eV binding energy.[28] The XPS analysis showed that doublets observed at higher binding energies (182.2/184.63 eV) were attributed to Zr^{3+} cations. Figure 1(e) shows that the Hf 4f spectrum of the HfAlO$_X$ layer can be deconvoluted into two groups of peaks. Peak positions of Hf 4f$_{7/2}$ and Hf 4f$_{5/2}$ are at 17.4 and 18.4 eV, respectively. In addition, Fig. 1(f) shows that the Al 2p spectrum of the HfAlO$_X$ layer can be deconvoluted into one peak. The peak position of Al 2p is at 74.0 eV. Figures 1(d) and 1(g) show the XPS plots of the O 1s peak spectra of the ZrO$_X$ and HfAlO$_X$ layers. Furthermore, the O 1s peak indicates the presence of different oxygen species in each layer of the memristor. The O 1s peak can be broken down into two components, designated O$_L$ and O$_V$, respectively. The O$_L$ and O$_V$ peaks are related to lattice oxygen and non-lattice oxygen (oxygen vacancies). The concentration of O$_L$ and O$_V$ was calculated as the total area of both peaks divided by a single peak.[29] Based on the simulated spectra, the percentage of oxygen vacancies was calculated to be 16% in the top HfAlO$_X$ layer, whereas it was 26% in the ZrO$_X$ layer. The XPS analysis confirmed that the HfAlO$_X$ layer had a lower concentration of oxygen vacancies. The XPS analysis confirmed that the HfAlO$_X$ layer exhibited a lower concentration of oxygen vacancies.

B. Resistive switching characteristics

The RS properties of ZrO$_X$-based RRAMs rely on the electroforming process, which triggers the movement of oxygen ions and the creation of oxygen vacancies.[30] Figures S2(a) and S2(b) (the supplementary material) illustrate the typical I–V curves for the forming processes of 30 randomly selected cells. The I_{cc} values of 10 and 1 mA were set for the single-layer and bilayer devices, respectively. It should be noted that the single-layer memory devices exhibited gradual increases from the high-resistance state (HRS) to the low-resistance state (LRS) and required much higher voltages than the bilayer memory devices. On the other hand, when the HfAlO$_X$ layer was inserted, a low initial current was confirmed because the additional HfAlO$_X$ layer acted as a series resistance. The bilayer device also transitioned from the HRS to the intermediate resistive state (IRS) at a lower voltage and then changed abruptly to the LRS. As illustrated in Fig. S2(c) (the supplementary material), a higher forming voltage distribution of the single-layer ZrO$_X$-based device is observed in the range from 12.0 to 16.0 V. In contrast, the bilayer ZrO$_X$-based device exhibits a low forming voltage distribution in the range of 6.0 to 13.0 V. From the results of the forming I–V curves, as described previously in Fig. S2 (the supplementary material), the bilayer structure of the ZrO$_X$-based device allows lower power consumption due to the lower forming voltage and I_{cc}, which are crucial for RRAM device applications. Figure 2(a) illustrates the typical I–V curves of the single-layer Ti/ZrO$_X$/TiN and bilayer Ti/ZrO$_X$/HfAlO$_X$/TiN devices. The voltage sweep direction is clockwise, and both devices exhibit bipolar RS characteristics. Fifty consecutive DC switching cycles were applied using negative set and positive reset voltages of −2.0 and 2.8 V without I_{cc}, respectively. In addition, Fig. S3 (the supplementary material) shows the results of 250 DC cycles and the conductance distributions of eight randomly selected memory cells during the cycling test of the double-layer
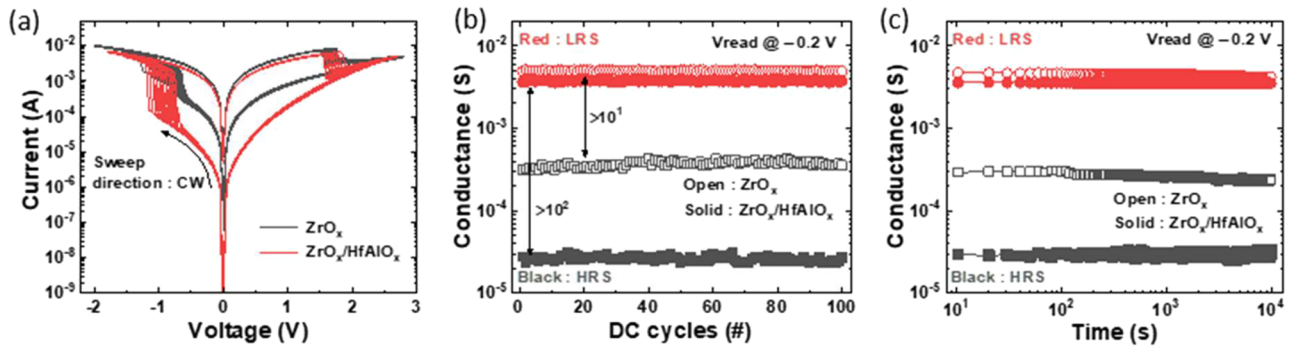
FIG. 2. (a) $I-V$ curves of ZrO$_X$ and ZrO$_X$/HfAlO$_X$-based devices for 50 cycles showing the self-compliance characteristic. (b) DC endurance and (c) retention performance.

RRAM device. It is very important for RRAM devices to operate reproducibly. To confirm that the bilayer device in this paper operates reproducibly, AC pulse endurance was additionally measured in addition to the existing DC 250 cycles. Based on the $I-V$ curve of the device to be measured, the pulse scheme, as shown in Fig. S3(c) (the supplementary material), consisted of a set pulse (-1.0 V), a read pulse (0.2 V), a reset pulse (2.0 V), and a read pulse (0.2 V) in one cycle. As it proceeded for a total of 10^3 times, the result is shown in the following figure: As shown in Fig. S3(d) (the supplementary material), the HRS was found to be worse than the initial state as it went on, but it was found to operate normally even after 10^3 attempts. In the SET process, both single-layer and bilayer devices are abruptly SET below -1.2 V, demonstrating self-compliant characteristics. In the RESET process, both devices are abruptly RESET below -2.0 V. The initial current in the bilayer device is lower than that in the single-layer device owing to the presence of the HfAlO$_X$ layer, which acts as a series resistance. Therefore, the bilayer device exhibits stronger RESET behavior than the single-layer device. In both the single-layer and bilayer devices, the self-compliance behaviors during the set transitions are attributed to the TiO$_X$ layer acting as an oxygen-ion reservoir that prevents current overshoot.[31] A DC endurance test and retention test were conducted to assess the device's performance. The endurance tests were carried out for

both the Ti/ZrO$_X$/TiN and Ti/ZrO$_X$/HfAlO$_X$/TiN devices at -0.2 V (V_{read}), as shown in Fig. 2(b). The HRS and LRS were maintained stably for 100 DC cycles, indicating excellent endurance characteristics for both devices. The on/off ratio for the Ti/ZrO$_X$/HfAlO$_X$/TiN device ($>10^2$) was higher than that of the Ti/ZrO$_X$/TiN device (>10). Retention tests were also performed to confirm the performances of the single-layer and bilayer devices, as shown in Fig. 2(c); both devices exhibited no degradation over 10^4 s. The bilayer device had a larger window than the single-layer device, similar to the endurance test results. The on/off ratio was significantly improved by the insertion of the HfAlO$_X$ layer without any degradation in retention.

Figure 3 shows the schematics of the CFs for the single-layer Ti/ZrO$_X$/TiN and bilayer Ti/ZrO$_X$/HfAlO$_X$/TiN structures based on the forming process and $I-V$ curve results. According to Gibbs's free energy theory, the RS mechanism of the ZrO$_X$-based RRAM devices can be explained by the exchange of oxygen between the HfO$_2$, ZrO$_2$, and TiO$_2$ layers. The Gibbs free energy values for oxide formation in ZrO$_2$, HfO$_2$, and TiO$_2$ are $\Delta G^o = -1100.0$ kJ/mol, $\Delta G^o = -1010.8$ kJ/mol, and $\Delta G^o = -888.0$ kJ/mol, respectively.[32] The lower Gibbs free energy value for ZrO$_2$ formation implies that it has more oxygen vacancies (V$_o$s) than HfO$_2$ and TiO$_2$.[33] Based on the XPS result as shown in Figs. 1(d) and 1(g), the ZrO$_X$ layer
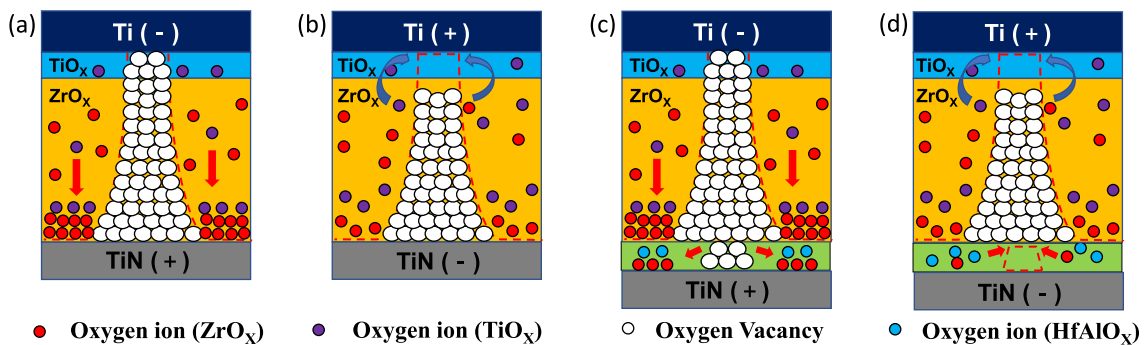
FIG. 3. Schematics of the RS mechanisms of the Ti/ZrO$_X$/TiN device for (a) LRS and (b) HRS, as well as the Ti/ZrO$_X$/HfAlO$_X$/TiN device for (c) LRS and (d) HRS.

contains a larger number of V_os than the TiO_X and $HfAlO_X$ layers. In addition, according to a prior study, the size of the CF was larger in an oxygen-deficient layer than in an oxygen-rich layer. When a high current is applied, the narrowest portion of the filament (in this study, the TiO_X/ZrO_X and $ZrO_X/HfAlO_X$ interface) heats up, allowing the migrated oxygen ions to reduce with the Joule heating effect and change LRS to HRS.[34,35] Given the above analysis, the SET process of the $Ti/ZrO_X/TiN$ device is shown in Fig. 3(a). This process involves applying a negative voltage to the Ti top electrode, which causes oxygen ions to move toward the bottom electrode and undergo reduction reactions, turning them into oxygen. This reaction causes the oxygen vacancies to gain two electrons and become neutral, creating CFs and putting the device in its LRS. Applying a positive voltage to the Ti top electrode during the RESET process makes it easy for the migrated oxygen ions to recombine (oxidize) with the oxygen vacancies at the TiO_X layer. This leads to the rupture of the CFs at the top interface region, as shown in Fig. 3(b). The formation of CFs in the bilayer structure is similar to that in the single-layer structure. However, the bilayer structure with additional $HfAlO_X$ shows a larger memory window than the single-layer structure, indicating that the $HfAlO_X$ layer is also involved in the formation of CFs. As depicted in Fig. 3(c), when a negative voltage is applied to the Ti top electrode, the oxygen ions migrate toward the TiN bottom electrode, leaving behind oxygen vacancies. This leads to the formation of CFs from the bottom to the top electrodes, resulting in device switching from the HRS to the LRS. As depicted in Fig. 3(d), when the TE is applied to opposing voltages during the RESET procedure, the CFs in the TiO_X and $HfAlO_X$ layers are ruptured, changing the device from HRS to LRS.

C. 1/f noise characteristics and transport mechanism

To investigate the current transport mechanism of the $Ti/ZrO_X/HfAlO_X/TiN$ RRAM device, we adopted a diagnosis tool using the $1/f$ noise measurement, which has been widely used as an assistive technique to analyze the transport mechanisms of RRAMs in previous studies.[36–38] Figure 4(a) shows the normalized noise power spectral density (S_I/I^2) for several devices for both the HRS and LRS of the $Ti/ZrO_X/HfAlO_X/TiN$ RRAM device. The S_I/I^2 is proportional to $1/f^\gamma$, with $\gamma \sim 1$ for both states except for the cell exhibiting random telegraph noise (RTN), which represents that low-frequency noise (LFN) characteristics in the $Ti/ZrO_X/HfAlO_X/TiN$ RRAM device also obey the classical $1/f$ noise theory. In the HRS of RRAM devices, the RTN is often observed.[39,40] RTN refers to the random fluctuation of the current level in the cell state. To ensure accurate analysis, cells that exhibit RTN during measurement were excluded from the interpretation of the experimental results. This exclusion helps to eliminate the influence of RTN on the observed data, allowing for a more reliable analysis of the experimental results. The noise power measured in the HRS is one order of magnitude higher than that in the LRS, as shown in Fig. 4(a). From
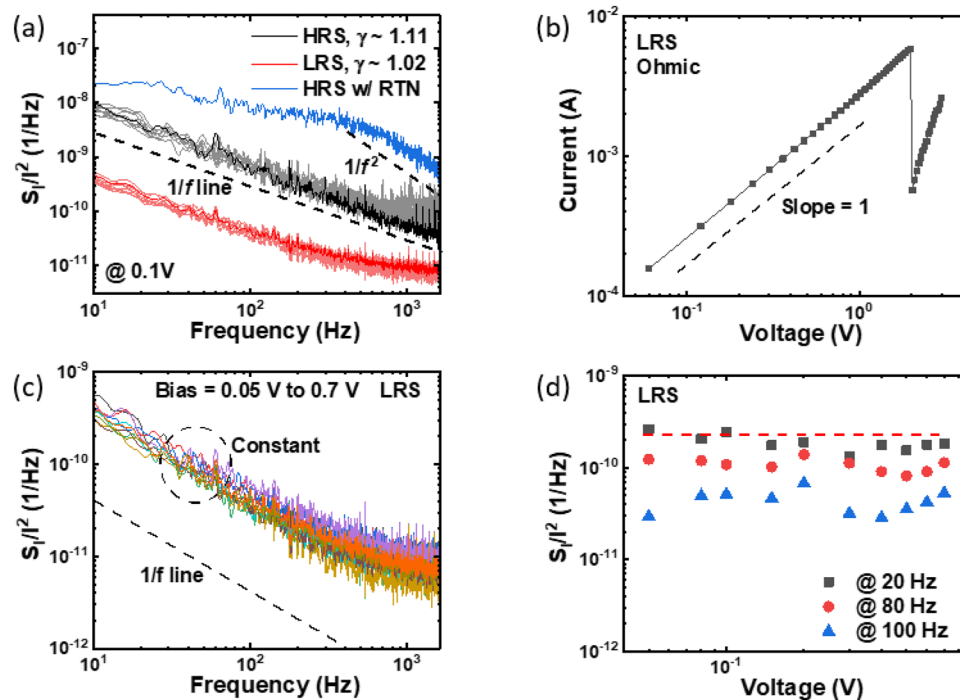
FIG. 4. (a) The S_I/I^2 for several devices for both the HRS and LRS of the $Ti/ZrO_X/HfAlO_X/TiN$ RRAM device. Note that the cell where RTN is observed does not follow the $1/f$ noise characteristic. (b) The $I-V$ curve of the LRS on a double-logarithmic scale, which fits well to a straight line of slope 1. (c) The S_I/I^2 measured at biases of 0.05–0.7 V in the LRS. (d) The voltage dependences of S_I/I^2 at frequencies of 20, 80, and 100 Hz in the LRS.

the comparison of the $1/f$ noise according to the resistance state, we estimate the localized conductive path in the RS layer. In the LRS, only the noise component associated with the localized path formed in the metal oxide exists, as depicted in Fig. 3(c). In contrast, in the HRS, the noise components resulting from various current paths within the broken gap are included, as shown in Fig. 3(d). Therefore, the noise level in the HRS is higher than that in the LRS.[41–43] The $I-V$ fitting method is the most commonly used approach to determine the transport mechanism of a device. Therefore, an initial step is to confirm the transport mechanism of the device via the $I-V$ fitting method. Figure 4(b) shows the $I-V$ curve of the LRS on a double-logarithmic scale, which fits well to a straight line of slope 1. This result shows that the dominant transport mechanism in the LRS is ohmic conduction, which is attributed to the percolation path formed in the forming and SET processes. Figure 4(c) shows the S_I/I^2 measured at biases of 0.05–0.7 V in the LRS. If the transport mechanism is ohmic, Hooge's empirical $1/f$ noise model can be applied.[39] This model is a universal empirical relation derived from noise measurements of different metal and semiconductor materials. The S_I/I^2 is defined as[44]

$$\frac{S_I}{I^2} = \frac{\alpha_H}{fN},\qquad(1)$$

where f is the frequency, α_H is the Hooge parameter, and N is the number of charge carriers. The bias dependence of S_I/I^2 can be used to confirm the current transport mechanism from Eq. (1). Figure 4(d) shows the voltage dependences of S_I/I^2 at frequencies of 20, 80, and 100 Hz in the LRS. The measured S_I/I^2 is nearly constant according to the voltage, which follows Hooge's empirical $1/f$ noise model. Therefore, the transport mechanism in the LRS is well supported by the noise measurement results. Figure 5(a) shows the fitting results for the Schottky (left) and Poole–Frenkel (PF) emission (right) models in the HRS. Schottky and PF emission are characterized by the semi-logarithmic plots of $I-V^{1/2}$ and I/V vs $V^{1/2}$, respectively.[45] Although the linearity is weak in the low voltage range, the straight lines in Fig. 5(a) suggest the possibility that the dominant transport mechanism in the HRS is Schottky or PF emission. Fig. S4 (the supplementary material) demonstrates the temperature-dependent proportional relationship between current density and voltage in HRS. Figure S4(a) (the supplementary material) corresponds to Schottky emission, while Fig. S4(b) (the supplementary material) corresponds to PF emission. The results obtained from temperature measurements also indicate the possibility of both emission mechanisms. Therefore, we reconfirmed the transport mechanism in the HRS with LFN measurements for accurate analysis. Figure 5(b) shows the S_I measured at biases of 0.1–1.0 V in the HRS. The noise model for Schottky emission can be expressed asfollows:[46]

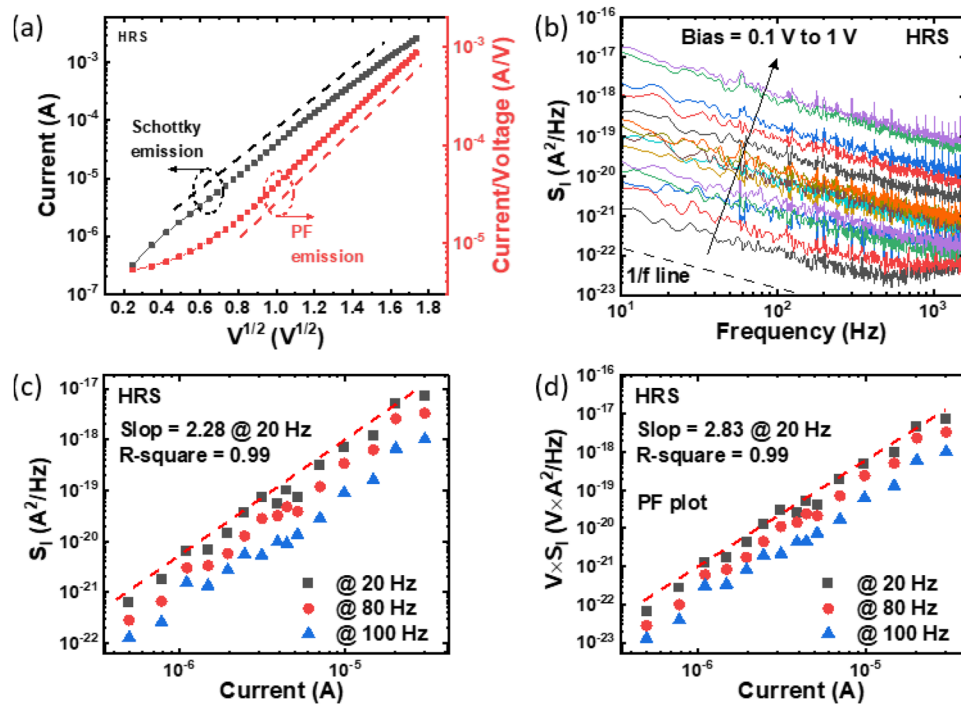$$S_I = \frac{k^*}{fA\exp(-qV_{bi}/k_BT)}I^2,\qquad(2)$$

FIG. 5. (a) The fitting results for the Schottky (left) and Poole–Frenkel (PF) emission (right) models in the HRS. (b) The S_I measured at biases of 0.1–1.0 V in the HRS. The fitting results for (c) Schottky and (d) PF emission.

where V_{bi} is the built-in potential of the Schottky contact and k^* is the fitting parameter that considers surface recombination velocity. The noise model of PF emission is given as follows:[47]

$$E \times S_I = \frac{\beta^2 N_D q^2 A}{\varepsilon^2 WLf} I^2, \tag{3}$$

where N_D is the trap density, ε is the permittivity, β is the PF fitting parameter, and A is the ratio of the trap's time constants, which in practical cases has the value of 0.1.[48] To confirm the bias dependence of the noise power, the S_I according to current is plotted on a double-logarithmic scale at frequencies of 20, 80, and 100 Hz, as shown in Fig. 5(c). The slope extracted from the linear fitting is 2.28, and the R-square value is 0.99. Hence, the S_I is approximately proportional to I^2 in all current ranges, which is in agreement with the $1/f$ noise model for Schottky emission.[46] Figure 5(d) shows the fitting results for PF emissions. According to the $1/f$ noise model for PF emission, the slope for the plot of $V \times S_I$ vs I on a double-log scale should be 2.[47] The slope extracted from the linear fitting is 2.83, and the R-square value is 0.99. Consequently, we conclude that the dominant transport mechanism in the HRS is Schottky emission from the I–V fitting and noise measurements.

D. Feasibility of the multi-level cell (MLC) operation

From a practical standpoint, the concept of multilevel memory is a fabulous approach to overcoming low-density memory limitations and creating connections between the memory and neuromorphic synapses.[49] In general, the multi-level cell (MLC) operation of the memristor can be obtained by adjusting the reset voltage, or I_{cc}. By adjusting the reset voltage, it is possible to control the gap between the electrode and the residual filament in the switching material. Otherwise, the lateral volume of the filament is controlled by changing the I_{cc}.[50] Due to the abrupt reset characteristics of the fabricated device, the MLC operation seems easier in the I_{cc} control mode. Figure 6(a) shows the I–V curves measured by adjusting I_{cc} from 500 μA to 6 mA during the SET process. Representative I–V curves for each I_{cc} are highlighted in color. As shown in Fig. 6(b), an MLC endurance test was conducted to confirm the possibility of multi-bit operation. Although there are overlapping parts among the seven cell states, a 2 bit operation (four-levels) was successfully achieved without any overlap. To examine the stability of each cell

state, MLC retention characteristics were measured for up to 10^4 s. As shown in Fig. 6(c), the cell states were maintained without any noticeable degradation.

E. Synaptic functionality

For the implementation of neuromorphic systems, it is essential to effectively mimic the function of biological synapses using artificial synapses. Among the various devices being studied, memristors, which are two-terminal devices, are structurally the most similar to biological synapses, and it has been proven that various functions can be imitated.[51] As shown in Fig. 7(a), in a biological neural system, presynaptic and postsynaptic neurons are connected through synapses. To transmit information from presynaptic neurons to postsynaptic neurons, presynaptic neurons first fire ions, which control the synaptic weight between neurons. When an action potential reaches a presynaptic neuron, the neurotransmitters are released into the synapse gap by diffusion of Ca^{2+} ions and are received by neuroreceptors on postsynaptic neurons.[52] In this process of nervous system interaction, synapses are where neurons are functionally connected and are a key component of information transmission. This phenomenon can be modeled with a two-terminal memristor, and top/bottom electrodes, pulse input signals applied to the electrode, and conductance changes of the switching material according to pulse stimulation are counterparts of each element of the biological synapse, as shown in Fig. 7(b).[51] In neuroscience, synaptic plasticity is attributed to the ability to change the strength and weight of connections between neurons, and this comes in different forms depending on the shape and timing of external stimuli.[53] Different types of plasticity are well described in Hebbian theory,[54,55] and representative synaptic behaviors include paired-pulse facilitation/depression, short- and long-term potentiation/depression, spike-number-dependent plasticity (SNDP), and spike-timing-dependent plasticity (STDP). Of these, STDP is considered the most central learning mechanism in Hebbian theory and plays an important role in information coding, learning, and memory.[56]

STDP is a synaptic learning rule in the human brain that adjusts the connection strength between neurons based on whether spikes occur simultaneously or at regular time intervals.[57,58] Figure S5(a) (the supplementary material) shows the schematic of spike pulses.
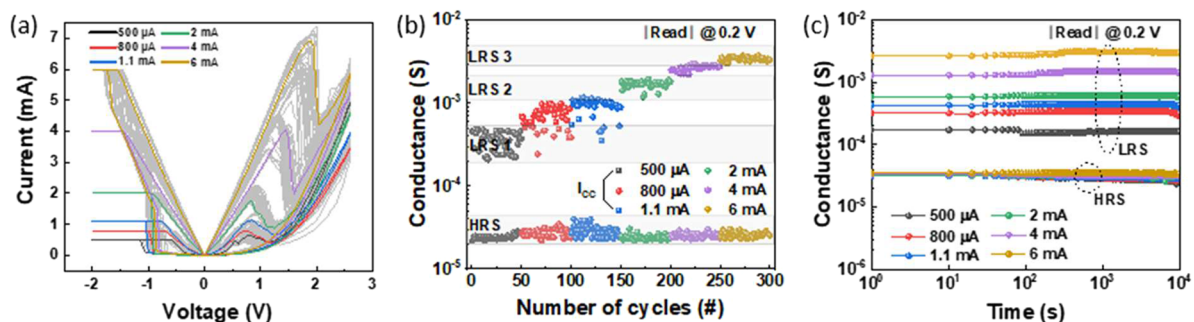

FIG. 6. Multilevel RS characteristics of the Ti/ZrO$_X$/HfAlO$_X$/TiN memristor: (a) I–V curves for different values of I_{cc}. (b) MLC endurance performance. 2 bit operations (four levels) are possible without any overlap. (c) MLC retention characteristics. The cell states were maintained without any noticeable degradation.
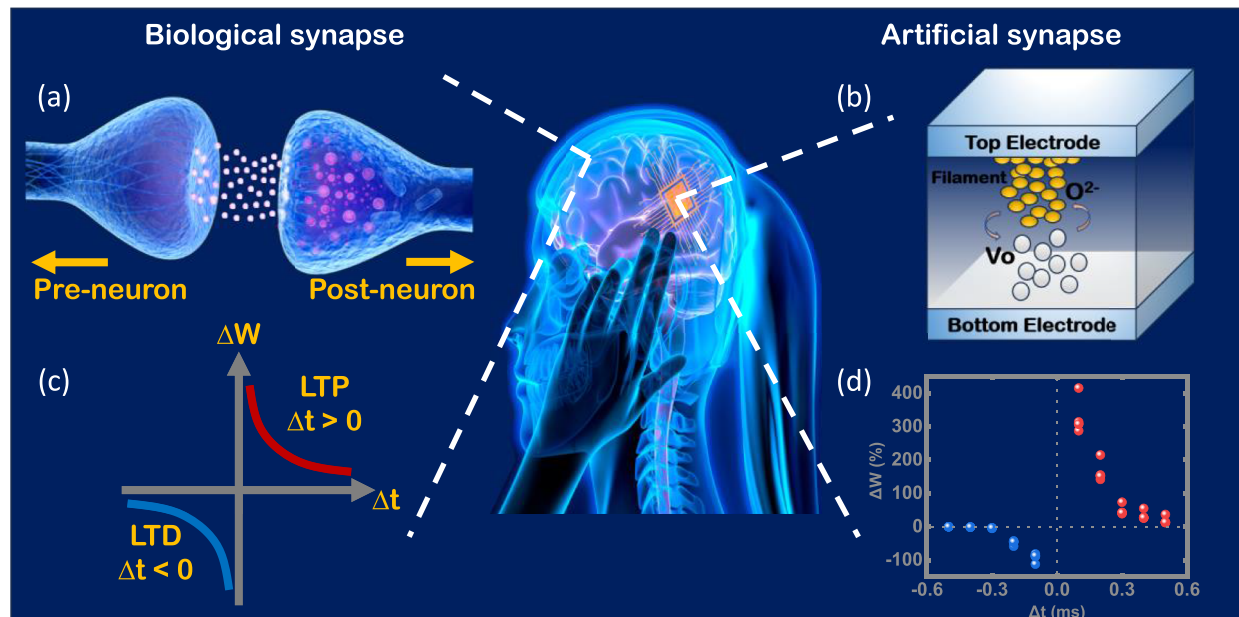
FIG. 7. Comparison of biological and artificial synapse. (a) The biological nervous system consists of pre- and post-synaptic neurons interconnected through synapses. (b) The memristor, which can mimic the function of the biological synapse. (c) The classical STDP curve originally described by Bi and Poo. (d) Measured conductance change as a function of the spike delay Δt, indicating potentiation for $\Delta t > 0$ and depression for $\Delta t < 0$.

In STDP, the change in synaptic weight is the function of relative neuron spike timing Δt ($\Delta t = t_{post} - t_{pre}$), where t_{pre} is the time when the presynaptic neuron spike arrives and t_{post} is the time when the postsynaptic neuron spike arrives. If the postsynaptic neuron spike arrives after the presynaptic neuron spike ($\Delta t > 0$), the synaptic weight increases, while if Δt is negative, i.e., the pre-spike follows the post-spike, then the synaptic weight decreases. The classical STDP curve originally described by Bi and Poo is depicted in Fig. 7(c).[59] In an artificial synapse based on a memristor, electrical pulse signals (spikes) can be applied to the memristor through the two electrodes and cause a modulation of the conductance of the memristor depending on the amplitude and relative timing of the pulses. That is, it is possible to realize the STDP function similar to the biological synapse systems. To provide an apparent demonstration of this phenomenon within our device, we executed a precisely calibrated application of a designed pulse stimulus to both the pre-synaptic and post-synaptic terminals of the Ti/ZrO$_X$/HfAlO$_X$/TiN device. Figure S5(b) (the supplementary material) shows the pulse schemes applied to our memristor. As shown in Fig. 7(d), when $\Delta t > 0$, the conductance (G) of the device gradually increases. On the other hand, when $\Delta t < 0$, the G value of the device gradually decreases. This tendency of synaptic weight change (ΔW) measured in our memristor is in good agreement with that of biological synapses, which confirms the feasibility of our device for neuromorphic computing applications. STDP data points (five cycles) in Fig. 7(d) have a remarkable statistical scatter, which has also been observed in the biological synapses. Herein, the ΔW is defined by $\Delta W = (G_{after} - G_{before})/G_{min}$ (after or before) $\times 100\%$, where G_{after} and G_{before} are conductances in the memristor before and after presynaptic and postsynaptic pulses are applied.[60]

To further evaluate the suitability of the Ti/ZrO$_X$/HfAlO$_X$/TiN device as a neuromorphic system, the potentiation and depression characteristics were examined. Potentiation and depression are dynamic states that manifest as alterations in synaptic potential in response to synaptic spikes. Potentiation corresponds to the strengthening of synaptic connectivity, promoting enhanced signal transmission. Conversely, depression represents the weakening of synaptic connectivity, leading to diminished signal transmission. These principles find application in the field of neuromorphic computing, where they serve as critical technologies to augment the learning and reasoning capabilities of artificial neural networks.[47,61] As depicted in Fig. S6(a) (the supplementary material), the potentiation was achieved by applying 50 identical pulses with an amplitude of -1.0 V and a width of 1 μs. Conversely, the depression was induced by applying 50 identical pulses with an amplitude of 1.2 V and a width of 1 μs. To ensure that the conductance was not affected during the read process, a low read pulse of 0.1 V was used during both potentiation and depression. Given that the conductance changes dramatically during the DC $I-V$ sweep, a sharp change in conductance can be seen after applying the first pulse for both potentiation and depression, as shown in Fig. 8(a). In applying 50 repetitive potentiation and depression pulses for ten cycles, constant HRS and LRS conductance values are maintained without any degradation over these ten cycles. However, the abrupt conductance changes in the identical pulses are not suitable for neuromorphic systems that require high accuracy for pattern recognition.[62,63] To
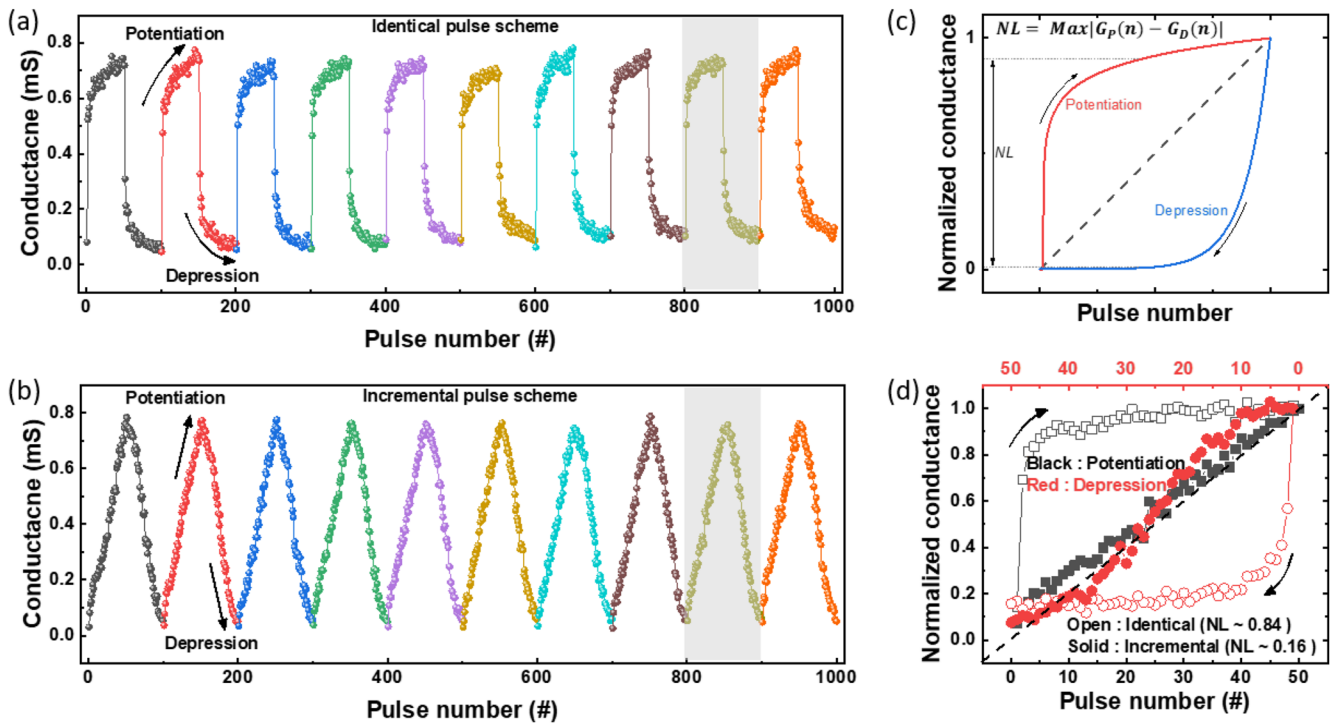
FIG. 8. Results of potentiation and depression measured in the bilayer device for ten pulse cycles using (a) an identical pulse and (b) an incremental pulse. (c) Non-linear conductance modulation curve with typical potentiation (red)/depression (blue) curves and normalized conductance as the Y-axis. The linear dashed line is an ideal case. (d) The comparison of nonlinearity for ninth potentiation/depression synaptic plasticity [gray part in Figs. 7(a) and 7(b)] with identical (open symbol) and incremental (solid symbol) pulses.

achieve linear and symmetric weights, an incremental pulse was constructed to achieve multiple weights. This pulse involves gradually ramping up the pulse conditions, thereby controlling the abrupt conductance changes in the identical pulses by gradually forming a filament and inducing a rupture. An incremental pulse scheme is shown in Fig. S6(b) (the supplementary material), where both potentiation and depression use a fixed pulse width of 1 μs. The amplitude was divided into 50 pulses for potentiation with a decline of 8.33 mV from −0.8 to −1.2 V and for depression with an increment of 8.33 mV from 1.0 to 1.4 V. Figure 8(b) shows the results of potentiation and depression for ten cycles when incremental pulses were applied. Compared to the result of applying identical pulses, the nonlinearity (NL) and symmetric conductance changes were greatly improved, and almost linear behavior was obtained. To evaluate the degree of improvement more quantitatively, we extracted the NL factor. The NL value can be expressed as the maximum value of the difference in conductance values normalized to the total plasticity during potentiation and depression, as shown in Fig. 8(c). The concept of NL proposed by Wang et al. is given as follows:[64]

$$NL = \max|G_P(n) - G_D(n)|, \quad n = 1, 2, 3, \ldots, N, \qquad (4)$$

where $G_P(n)$ and $G_D(n)$ are the normalized conductance values, which are from 0 to 1, and n is the pulse number. By definition, it is most desirable for NL to be zero, as shown in the linear dashed

line of Fig. 8(c), because linear weight update is the most ideal in hardware-based neuromorphic system development. Figure 8(d) shows the normalized conductance vs pulse number during potentiation (black) and depression (red) for the ninth cycle with identical (open symbol) and incremental (solid symbol) pulses applied. From Eq. (4), NL values of 0.81 and 0.1 were extracted for identical and incremental pulses, respectively. That is, linearity and symmetry are greatly improved with amplitude modulation. Referring to the DC $I–V$ curves, it becomes evident that abrupt switching behavior is present. To suppress this behavior and prevent sudden changes in conductance, it is advised to initiate the process with a small voltage, reducing the NL.

Moreover, based on the result of 50 repetitive potentiation and depression pulses for ten cycles, incremental pulses were possible to regulate the sudden changes in conductance observed for the identical pulses; this was achieved by gradually developing a filament and causing a rupture in the system. To test the accuracy of pattern recognition, we conducted an MNIST simulation using Python. As shown in Fig. 9(a), our assumption was that the pixel values of a 28 × 28 image would change based on the results of potentiation and depression. The normalization equation can be expressed as follows:

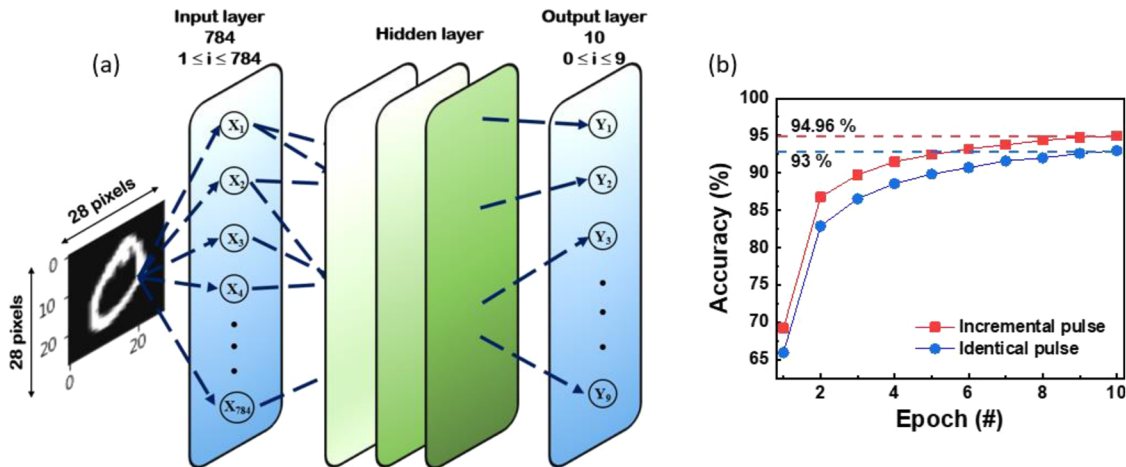$$\omega = \frac{G - G_{\min}}{G_{\max} - G_{\min}} \qquad (5)$$

FIG. 9. (a) Neural network framework for MNIST pattern recognition simulation. (b) The accuracy of pattern recognition over ten consecutive epochs at an incremental and identical pulse.

with G_{max} and G_{min} representing the maximum and minimum conductivity in each graph, respectively.[65,66] As the potentiation and depression pulses are applied, the conductance value according to each pulse appears. At this time, normalization was performed on the conductance value G, and MNIST simulation was performed on the synaptic weight (ω) value. Synaptic weights are matched for each layer, and the weight values are adjusted as the MINST simulation progresses to reduce the error between input and output.[67] The reason for normalization is that neural networks often use activation functions [e.g., sigmoid and rectified linear unit (ReLU)] that are sensitive to the input range. Normalizing the conductance values can prevent issues such as vanishing gradients or exploding gradients during backpropagation, which can occur when the input values are too large or too small. Currently, the equation for normalization is the same as Eq. (5), where G means the conductance for one pulse number, G_{max} means the maximum conductance in the graph, and G_{min} means the minimum conductance in the graph. When the pixel value of the next image needed to increase, we followed the potentiation graph, and in the opposite case, we followed the depression graph. This resulted in fewer image modifications when the potentiation and depression graphs were symmetrical and linear. Image training was conducted 60 000 times using 784 input neurons and systematically hidden layers. Hidden layers were used in the dense neural network (DNN) method. Hidden layers consist of three layers: the first layer consists of 128 neurons, the second layer consists of 64 neurons, and the third layer consists of 32 neurons. Each layer uses ReLU as an activation function. After passing through three hidden layers, the result of each output layer from 0 to 9 is expressed as a probability using the softmax function. By repeatedly performing this process, MNIST accuracy values are obtained based on the modifications of each potentiation and depression. Finally, we confirmed the results with ten output neurons. In Fig. 9(b), we used 10 000 ideal images that had not been modified as test images and performed ten epochs, achieving an accuracy of 93.00% for identical pulses and 94.96% for incremental pulses.

IV. CONCLUSION

This study compares the resistance and synaptic properties of Ti/ZrO$_X$/TiN and Ti/ZrO$_X$/HfAlO$_X$/TiN RRAM devices. In the case of the Ti/ZrO$_X$/HfAlO$_X$/TiN device, the thin HfAlO$_X$ layer acts as a series resistance that reduces the operating current. Therefore, it has advantages in terms of accuracy in distinguishing the on/off state and power consumption by having a lower operating current. We also clarify the transport mechanism in the Ti/ZrO$_X$/HfAlO$_X$/TiN device by LFN measurements. Furthermore, the MLC characteristics, potentiation, and depression were examined. An incremental pulse was used to adjust numerous synaptic weights to improve the precision of an artificial neural network. Finally, we evaluated the capability of the Ti/ZrO$_X$/HfAlO$_X$/TiN device to function as a neuromorphic device by examining its pattern recognition accuracy using MNIST results.

SUPPLEMENTARY MATERIAL

The supplementary material includes the distribution of electrical characteristics, the results of temperature measurements, and the pulse schemes for measurements of synaptic functions.

AUTHOR DECLARATIONS

Conflict of Interest

The authors have no conflicts to disclose.

Author Contributions

J.H. and Y.C. contributed equally to this work.

Jungang Heo: Conceptualization (lead); Data curation (lead); Formal analysis (lead); Investigation (lead); Methodology (lead); Writing – original draft (lead). **Youngboo Cho**: Data curation (lead); Formal analysis (lead); Investigation (lead); Writing – original draft (lead). **Hyeonseung Ji**: Investigation (supporting); Writing – original draft (supporting). **Min-Hwi Kim**: Conceptualization (supporting); Methodology (supporting); Validation (supporting). **Jong-Ho Lee**: Methodology (supporting); Supervision (supporting); Validation (supporting). **Jung-Kyu Lee**: Data curation (lead); Investigation (lead); Methodology (lead); Supervision (equal); Validation (equal); Visualization (lead); Writing – original draft (lead). **Sungjun Kim**: Conceptualization (lead); Funding acquisition (lead); Project administration (lead); Resources (lead); Supervision (lead); Validation (lead).

DATA AVAILABILITY

The data that support the findings of this study are available within the article and its supplementary material and from the corresponding authors upon reasonable request.

REFERENCES

[1]V. Milo, C. Zambelli, P. Olivo, E. Pérez, M. K. Mahadevaiah, O. G. Ossorio, C. Wenger, and D. Ielmini, "Multilevel HfO_2-based RRAM devices for low-power neuromorphic networks," APL Mater. **7**(8), 081120 (2019).

[2]M. Hu, C. E. Graves, C. Li, Y. Li, N. Ge, E. Montgomery, N. Davila, H. Jiang, R. S. Williams, J. J. Yang, Q. Xia, and J. P. Strachan, "Memristor-based analog computation and neural network classification with a dot product engine," Adv. Mater. **30**(9), 1705914 (2018).

[3]B. Sun, T. Guo, G. Zhou, S. Ranjan, Y. Jiao, L. Wei, Y. N. Zhou, and Y. A. Wu, "Synaptic devices based neuromorphic computing applications in artificial intelligence," Mater. Today Phys. **18**, 100393 (2021).

[4]R. Martins, P. Barquinha, L. Pereira, N. Correia, G. Gonçalves, I. Ferreira, and E. Fortunato, "Selective floating gate non-volatile paper memory transistor," Phys. Status Solidi RRL **3**(9), 308–310 (2009).

[5]Z. Wang, H. Wu, G. W. Burr, C. S. Hwang, K. L. Wang, Q. Xia, and J. J. Yang, "Resistive switching materials for information processing," Nat. Rev. Mater. **5**(3), 173–195 (2020).

[6]J. Zhu, T. Zhang, Y. Yang, and R. Huang, "A comprehensive review on emerging artificial neuromorphic devices," Appl. Phys. Rev. **7**(1), 011312 (2020).

[7]M. Suri, V. Parmar, A. Kumar, D. Querlioz, and F. Alibart, in *2015 15th Non-Volatile Memory Technology Symposium (NVMTS)* (IEEE, 2015), pp. 1–6.

[8]G. Pedretti and D. Ielmini, "In-memory computing with resistive memory circuits: Status and outlook," Electronics **10**(9), 1063 (2021).

[9]M. Trapatseli, A. Khiat, S. Cortese, A. Serb, D. Carta, and T. Prodromakis, "Engineering the switching dynamics of TiO_x-based RRAM with Al doping," J. Appl. Phys. **120**(2), 025108 (2016).

[10]S. R. Lee, Y.-B. Kim, M. Chang, K. M. Kim, C. B. Lee, J. H. Hur, G.-S. Park, D. Lee, M.-J. Lee, C. J. Kim, U.-I. Chung, I.-K. Yoo, and K. Kim, in *2012 Symposium on VLSI Technology (VLSIT)* (IEEE, 2012), pp. 71–72.

[11]C.-Y. Liu, J.-Y. Ho, J.-J. Huang, and H.-Y. Wang, "Transient current of resistive switching of a NiO_x resistive memory," Jpn. J. Appl. Phys. **51**(4R), 041101 (2012).

[12]S. R. Patil, M. Y. Chougale, T. D. Rane, S. S. Khot, A. A. Patil, O. S. Bagal, S. D. Jadhav, A. D. Sheikh, S. Kim, and T. D. Dongale, "Solution-processable ZnO thin film memristive device for resistive random access memory application," Electronics **7**(12), 445 (2018).

[13]Z. J. Shen, C. Zhao, C. Z. Zhao, I. Z. Mitrovic, L. Yang, W. Y. Xu, E. G. Lim, T. Luo, and Y. B. Huang, in *2019 International Conference on IC Design and Technology (ICICDT)* (IEEE, 2019), pp. 1–4.

[14]C. Kim, Y. Lee, S. Kim, M. Kang, and S. Kim, "Diverse synaptic weight adjustment of bio-inspired ZrO_x-based memristors for neuromorphic system," Mater. Sci. Semicond. Process. **157**, 107314 (2023).

[15]Y. Tao, W. Ding, Z. Wang, H. Xu, X. Zhao, X. Li, W. Liu, J. Ma, and Y. Liu, "Improved switching reliability achieved in HfO_x based RRAM with mountain-like surface-graphited carbon layer," Appl. Surf. Sci. **440**, 107–112 (2018).

[16]Z. Shen, C. Zhao, Y. Qi, W. Xu, Y. Liu, I. Z. Mitrovic, L. Yang, and C. Zhao, "Advances of RRAM devices: Resistive switching mechanisms, materials and bionic synaptic application," Nanomaterials **10**(8), 1437 (2020).

[17]S. K. Vishwanath, H. Woo, and S. Jeon, "Enhancement of resistive switching properties in Al_2O_3 bilayer-based atomic switches: Multilevel resistive switching," Nanotechnology **29**(23), 235202 (2018).

[18]C. Ye, T. Deng, J. Zhang, L. Shen, P. He, W. Wei, and H. Wang, "Enhanced resistive switching performance for bilayer HfO_2/TiO_2 resistive random access memory," Semicond. Sci. Technol. **31**(10), 105005 (2016).

[19]J. Lee, E. M. Bourim, W. Lee, J. Park, M. Jo, S. Jung, J. Shin, and H. Hwang, "Effect of ZrO_x/HfO_x bilayer structure on switching uniformity and reliability in nonvolatile memory applications," Appl. Phys. Lett. **97**(17), 172105 (2010).

[20]A. S. Sokolov, S. K. Son, D. Lim, H. H. Han, Y.-R. Jeon, J. H. Lee, and C. Choi, "Comparative study of Al_2O_3, HfO_2, and $HfAlO_x$ for improved self-compliance bipolar resistive switching," J. Am. Ceram. Soc. **100**(12), 5638–5648 (2017).

[21]H. Ryu, J. Choi, and S. Kim, "Voltage amplitude-controlled synaptic plasticity from complementary resistive switching in alloying HfO_x with AlO_x-based RRAM," Metals **10**(11), 1410 (2020).

[22]Y.-J. Lin, W.-C. Chen, Y.-M. Chin, and C.-J. Liu, "Hysteresis mechanism in current–voltage characteristics of ZrO_x films prepared by the sol–gel method," J. Phys. D: Appl. Phys. **42**(4), 045419 (2009).

[23]I. A. Surazhevsky, V. A. Demin, A. I. Ilyasov, A. V. Emelyanov, K. E. Nikiruy, V. V. Rylkov, S. A. Shchanikov, I. A. Bordanov, S. A. Gerasimova, D. V. Guseinov, N. V. Malekhonova, D. A. Pavlov, A. I. Belov, A. N. Mikhaylov, V. B. Kazantsev, D. Valenti, B. Spagnolo, and M. V. Kovalchuk, "Noise-assisted persistence and recovery of memory state in a memristive spiking neuromorphic network," Chaos, Solitons Fractals **146**, 110890 (2021).

[24]J.-K. Lee, S. Jung, J. Park, S.-W. Chung, J. Sung Roh, S.-J. Hong, I. Hwan Cho, H.-I. Kwon, C. Hyeong Park, B.-G. Park, and J.-H. Lee, "Accurate analysis of conduction and resistive-switching mechanisms in double-layered resistive-switching memory devices," Appl. Phys. Lett. **101**(10), 103506 (2012).

[25]R.-H. Koo, W. Shin, K. K. Min, D. Kwon, D. H. Kim, J.-J. Kim, D. Kwon, and J.-H. Lee, "Effect of carrier transport process on tunneling electroresistance in ferroelectric tunnel junction," IEEE Electron Device Lett. **44**(1), 164–167 (2023).

[26]R.-H. Koo, W. Shin, K. K. Min, D. Kwon, J.-J. Kim, D. Kwon, and J.-H. Lee, "Optimizing post-metal annealing temperature considering different resistive switching mechanisms in ferroelectric tunnel junction," IEEE Electron Device Lett. **44**(6), 935–938 (2023).

[27]W. Shin, K. K. Min, J.-H. Bae, J. Kim, R.-H. Koo, D. Kwon, J.-J. Kim, D. Kwon, and J.-H. Lee, "1/f noise in synaptic ferroelectric tunnel junction: Impact on convolutional neural network," Adv. Intell. Syst. **5**(6), 2200377 (2023).

[28]Z. Azdad, L. Marot, L. Moser, R. Steiner, and E. Meyer, "Valence band behaviour of zirconium oxide, Photoelectron and Auger spectroscopy study," Sci. Rep. **8**(1), 16251 (2018).

[29]Y. Tu, S. Chen, X. Li, J. Gorbaciova, W. P. Gillin, S. Krause, and J. Briscoe, "Control of oxygen vacancies in ZnO nanorods by annealing and their influence on ZnO/PEDOT:PSS diode behaviour," J. Mater. Chem. C **6**(7), 1815–1821 (2018).

[30]C.-C. Hsu, T.-C. Wang, and C.-C. Tsao, "Forming-free sol-gel ZrO_x resistive switching memory," J. Alloys Compd. **769**, 65–70 (2018).

[31]H. Jeon, J. Park, W. Jang, H. Kim, C. Kang, H. Song, H. Kim, H. Seo, and H. Jeon, "Stabilized resistive switching behaviors of a $Pt/TaO_x/TiN$ RRAM under different oxygen contents," Phys. Status Solidi A **211**(9), 2189–2194 (2014).

[32]M. Ismail, Z. Batool, K. Mahmood, A. Manzoor Rana, B.-D. Yang, and S. Kim, "Resistive switching characteristics and mechanism of bilayer HfO_2/ZrO_2 structure deposited by radio-frequency sputtering for nonvolatile memory," Results Phys. **18**, 103275 (2020).

[33]C.-A. Lin, C.-J. Huang, and T.-Y. Tseng, "Impact of barrier layer on HfO_2-based conductive bridge random access memory," Appl. Phys. Lett. **114**(9), 093105 (2019).

[34]T.-L. Tsai, H.-Y. Chang, J. J.-C. Lou, and T.-Y. Tseng, "A high performance transparent resistive switching memory made from ZrO_2/AlON bilayer structure," Appl. Phys. Lett. **108**(15), 153505 (2016).

[35]M.-H. Lin, M.-C. Wu, C.-Y. Huang, C.-H. Lin, and T.-Y. Tseng, "High-speed and localized resistive switching characteristics of double-layer $SrZrO_3$ memory devices," J. Phys. D: Appl. Phys. **43**(29), 295404 (2010).

[36]B. Das, A. Bera, M. Samanta, S. Bera, S. Kalimuddin, M. Kundu, S. Gayen, K. K. Chattopadhyay, and M. Mondal, "Resistive switching in a $MoSe_2$-based memory device investigated using conductance noise spectroscopy," ACS Appl. Electron. Mater. **3**(7), 3096–3105 (2021).

[37]J.-K. Lee, H. Y. Jeong, I.-T. Cho, J. Y. Lee, S.-Y. Choi, H.-I. Kwon, and J.-H. Lee, "Conduction and low-frequency noise analysis in Al/α-TiO_X/Al bipolar switching resistance random access memory devices," IEEE Electron Device Lett. **31**(6), 603–605 (2010).

[38]F. N. Hooge, "1/f noise," Physica B+C **83**(1), 14–23 (1976).

[39]J. Lee, J. Shin, D. Lee, W. Lee, S. Jung, M. Jo, J. Park, K. P. Biju, S. Kim, S. Park, and H. Hwang, in *2010 International Electron Devices Meeting* (IEEE, 2010), pp. 19.5.1–19.5.4.

[40]J.-K. Lee, J.-W. Lee, J. Park, S.-W. Chung, J. S. Roh, S.-J. Hong, I. Cho, H.-I. Kwon, and J.-H. Lee, "Extraction of trap location and energy from random telegraph noise in amorphous TiO_x resistance random access memories," Appl. Phys. Lett. **98**(14), 143502 (2011).

[41]Z. Fang, H. Y. Yu, J. A. Chroboczek, G. Ghibaudo, J. Buckley, B. DeSalvo, X. Li, and D. L. Kwong, "Low-frequency noise in oxide-based (TiN/HfO_x/Pt) resistive random access memory cells," IEEE Trans. Electron Devices **59**(3), 850–853 (2012).

[42]J.-K. Lee, S. Jung, B.-I. Choe, J. Park, S.-W. Chung, J. S. Roh, S.-J. Hong, C. H. Park, B.-G. Park, and J.-H. Lee, "Flicker noise behavior in resistive memory devices with double-layered transition metal oxide," IEEE Electron Device Lett. **34**(2), 244–246 (2013).

[43]Y. Lee, J. Park, D. Chung, K. Lee, and S. Kim, "Multi-level cells and quantized conductance characteristics of Al_2O_3-based RRAM device for neuromorphic system," Nanoscale Res. Lett. **17**(1), 84 (2022).

[44]F.-C. Chiu, "A review on conduction mechanisms in dielectric films," Adv. Mater. Sci. Eng. **2014**, 578168.

[45]C. H. Park and J.-H. Lee, "Formulas of 1/f noise in Schottky barrier diodes under reverse bias," Solid-State Electron. **69**, 85–88 (2012).

[46]J.-K. Lee, I.-T. Cho, H.-I. Kwon, C. S. Hwang, C. H. Park, and J.-H. Lee, "Relationship between conduction mechanism and low-frequency noise in polycrystalline- TiO_x-based resistive-switching memory devices," IEEE Electron Device Lett. **33**(7), 1063–1065 (2012).

[47]W. Shin, K. K. Min, J.-H. Bae, J. Yim, D. Kwon, Y. Kim, J. Yu, J. Hwang, B.-G. Park, D. Kwon, and J.-H. Lee, "Comprehensive and accurate analysis of the working principle in ferroelectric tunnel junctions using low-frequency noise spectroscopy," Nanoscale **14**(6), 2177–2185 (2022).

[48]C. T. Angelis, C. A. Dimitriadis, I. Samaras, J. Brini, G. Kamarinos, V. K. Gueorguiev, and T. E. Ivanov, "Study of leakage current in n-channel and p-channel polycrystalline silicon thin-film transistors by conduction and low frequency noise measurements," J. Appl. Phys. **82**(8), 4095–4101 (1997).

[49]H. Kang, J. Park, D. Lee, H. W. Kim, S. Jin, M. Ahn, and J. Woo, "Two- and three-terminal HfO_2-based multilevel resistive memories for neuromorphic analog synaptic elements," Neuromorphic Comput. Eng. **1**(2), 021001 (2021).

[50]A. Prakash and H. Hwang, "Multilevel cell storage and resistance variability in resistive random access memory," Phys. Sci. Rev. **1**(6), 20160010 (2016).

[51]S. Yang, T. Kim, S. Kim, D. Chung, T.-H. Kim, J.-K. Lee, S. Kim, M. Ismail, C. Mahata, S. Kim, and S. Cho, "Synaptic plasticity and non-volatile memory characteristics in TiN-nanocrystal-embedded 3D vertical memristor-based synapses for neuromorphic systems," Nanoscale **15**, 13239 (2023).

[52]S. Kim, C. Du, P. Sheridan, W. Ma, S. Choi, and W. D. Lu, "Experimental demonstration of a second-order memristor and its ability to biorealistically implement synaptic plasticity," Nano Lett. **15**(3), 2203–2211 (2015).

[53]E. Li, W. Lin, Y. Yan, H. Yang, X. Wang, Q. Chen, D. Lv, G. Chen, H. Chen, and T. Guo, "Synaptic transistor capable of accelerated learning induced by temperature-facilitated modulation of synaptic plasticity," ACS Appl. Mater. Interfaces **11**(49), 46008–46016 (2019).

[54]M. Tsodyks and C. Gilbert, "Neural networks and perceptual learning," Nature **431**(7010), 775–781 (2004).

[55]S. Song, K. D. Miller, and L. F. Abbott, "Competitive Hebbian learning through spike-timing-dependent synaptic plasticity," Nat. Neurosci. **3**(9), 919–926 (2000).

[56]W. Huang, X. Xia, C. Zhu, P. Steichen, W. Quan, W. Mao, J. Yang, L. Chu, and X. Li, "Memristive artificial synapses for neuromorphic computing," Nano-Micro Lett. **13**(1), 85 (2021).

[57]S. Bianchi, G. Pedretti, I. Muñoz-Martín, A. Calderoni, N. Ramaswamy, S. Ambrogio, and D. Ielmini, "A compact model for stochastic spike-timing-dependent plasticity (STDP) based on resistive switching memory (RRAM) synapses," IEEE Trans. Electron Devices **67**(7), 2800–2806 (2020).

[58]C. Mahata, M. Kang, and S. Kim, "Multi-level analog resistive switching characteristics in tri-layer HfO_2/Al_2O_3/HfO_2 based memristor on ITO electrode," Nanomaterials **10**(10), 2069 (2020).

[59]G. Bi and M. Poo, "Synaptic modifications in cultured hippocampal neurons: Dependence on spike timing, synaptic strength, and postsynaptic cell type," J. Neurosci. **18**(24), 10464–10472 (1998).

[60]T. Mazur, P. Zawal, and K. Szaciłowski, "Synaptic plasticity, metaplasticity and memory effects in hybrid organic–inorganic bismuth-based materials," Nanoscale **11**(3), 1080–1090 (2019).

[61]J.-K. Lee and S. Kim, "Comparative analysis of low-frequency noise based resistive switching phenomenon for filamentary and interfacial RRAM devices," Chaos, Solitons Fractals **173**, 113633 (2023).

[62]S. Kim, H. Kim, S. Hwang, M.-H. Kim, Y.-F. Chang, and B.-G. Park, "Analog synaptic behavior of a silicon nitride memristor," ACS Appl. Mater. Interfaces **9**(46), 40420–40427 (2017).

[63]Z. Wang, M. Yin, T. Zhang, Y. Cai, Y. Wang, Y. Yang, and R. Huang, "Engineering incremental resistive switching in TaO_X based memristors for brain-inspired computing," Nanoscale **8**(29), 14015–14022 (2016).

[64]I.-T. Wang, C.-C. Chang, L.-W. Chiu, T. Chou, and T.-H. Hou, "3D Ta/TaO_X/TiO_2/Ti synaptic array and linearity tuning of weight update for hardware neural network applications," Nanotechnology **27**(36), 365204 (2016).

[65]E. Covi, S. Brivio, M. Fanciulli, and S. Spiga, "Synaptic potentiation and depression in Al:HfO_2-based memristor," Microelectron. Eng. **147**, 41–44 (2015).

[66]J. Park, T.-H. Kim, O. Kwon, M. Ismail, C. Mahata, Y. Kim, S. Kim, and S. Kim, "Implementation of convolutional neural network and 8-bit reservoir computing in CMOS compatible VRRAM," Nano Energy **104**, 107886 (2022).

[67]J.-W. Jang, S. Park, G. W. Burr, H. Hwang, and Y.-H. Jeong, "Optimization of conductance change in $Pr_{1-X}Ca_XMnO_3$-based synaptic devices for neuromorphic systems," IEEE Electron Device Lett. **36**(5), 457–459 (2015).